Small molecule ensembles reshape amyloid aggregation landscapes

Radhika V. Nair[1], Bich Ngoc Tran[2], Atul N. Parikh[1], and Matthew R. Foreman[*1,3]

[1]Institute for Digital Molecular Analytics and Science, Nanyang Technological University, 59 Nanyang Drive, Singapore 636921, Singapore

[2]NTU Institute of Structural Biology (NISB), Nanyang Technological University, Experimental Medicine Building, 59 Nanyang Drive, Singapore 636921

[3]School of Electrical and Electronic Engineering, Nanyang Technological University, 50 Nanyang Avenue, Singapore 639798

Abstract

Amyloid-β_{42} assemblies form a dynamic network of oligomers and fibrils, with fibrillar species acting as reservoirs that maintain equilibrium among intermediates. Perturbing a single species shifts the oligomer-fibril balance, highlighting the challenge of selectively targeting toxic species while maintaining the dynamic equilibrium of the amyloid network. Here, we show that the small molecule EPPS (4-(2-hydroxyethyl)-1-piperazine-propanesulfonic acid) fine tunes this network through cooperative, concentration-dependent disaggregation. At optimal concentrations, EPPS efficiently shifts the equilibrium away from the fibrillar structures via multisite, allosteric interactions. At higher concentrations, EPPS self-assembles into supramolecular clusters, depleting free molecules and allowing partially disaggregated amyloid intermediates to reassemble. Notably, at elevated concentrations, interactions transition from molecule-to-molecule to higher-order ensemble-to-ensemble engagement, where EPPS clusters and amyloid fibrils mutually reshape each other's dynamics. Molecular crowding, modeled with polyethylene glycol, further restricts EPPS access to fibrillar surfaces, modulating activity. These findings reveal that small molecule dynamics, including cooperative binding, self-assembly, and environment-dependent accessibility, critically govern amyloid network control, providing a mechanistic blueprint for rational design of next-generation amyloid-targeting therapeutics.

*Corresponding author: matthew.foreman@ntu.edu.sg

Introduction

Amyloid-β (Aβ) peptides, 39-43 amino acids in length ($\sim$4 kDa), are generated by sequential cleavage of the amyloid precursor protein (APP, $\sim$120 kDa) by β- and γ-secretases [1]. Owing to the poor solubility in aqueous media, they readily self-associate both *in vivo* and *in vitro* producing structurally heterogeneous mixtures of higher-order, mesoscopic aggregates [2, 3]. These aggregates comprise a diverse variety of species, including β-sheet-rich oligomers, spherical non-β-sheet aggregates, micelles, protofibrils, and mature fibrils. Collectively, these species span a broad conformational phase space: some correspond to distinct on-pathway intermediates en route to fibril formation, whereas others, such as non-β-sheet aggregates that transiently sequester monomers or oligomers, represent off-pathway intermediates residing in local free-energy minima along side branches of the amyloid aggregation landscape [4, 5].

Rather than existing as isolated entities, these structurally diverse aggregates are dynamically interconnected, collectively forming an interconnected reaction network that underlies amyloid polymorphism, as illustrated in Figure 1. Each Aβ aggregate species therefore represent local nodes within an elaborate network linking monomers to mature fibrils across a rugged free-energy landscape. This network consists of multiple competing pathways, with nodes corresponding to local free-energy minima associated with distinct aggregation products. Within this reaction network, fibril formation proceeds predominantly along a canonical nucleation-dependent polymerization pathway. This self-assembly process comprises two phases: (1) a lag phase, during which stochastic association of soluble monomers overcomes an energy barrier to form a stable critical nucleus, and (2) an elongation phase, in which monomer (or oligomer) addition to fibril seeds is thermodynamically favored ($\Delta G < 0$) [6]. Beyond this dominant route, secondary nucleation and oligomer-fibril interactions introduce alternative side pathways that further diversify the aggregation free-energy landscape [7, 8, 9].

In living systems, the steady-state distribution of higher-order amyloids under any condition is shaped not only by aggregation but also by opposing disaggregation processes. Aβ aggregates are continually counterbalanced by these competing pathways, which are often mediated by molecule chaperons such as HSP70 and clusterin. Through fibril fragmentation and/or monomer release, they generate additional mesoscopic aggregates. A dynamic balance between the two - aggregation and disaggregation - thus governs amyloid turnover [10]. Disruption of this finely tuned balance, such as through proteostatic failure, oxidative stress, or aberrant membrane interactions, can shift the equilibrium toward the accumulation of neurotoxic species [11]. Conversely, deliberate exogenous perturbations that modulate aggregation or disaggregation kinetics can remodel the reaction network, redistributing the populations of mesoscopic amyloid aggregates and potentially restoring proteostasis. We therefore hypothesize that targeting this dynamic network, rather than individual species alone, hence offers promising therapeutic opportunities.

Viewed through this dynamic network perspective, existing therapeutic approaches can be broadly classified into two strategies: early suppression of aggregation process [12] and enhancement of disaggregation pathways [13]. For the former, small molecules such as polyphenols (e.g., EGCG and

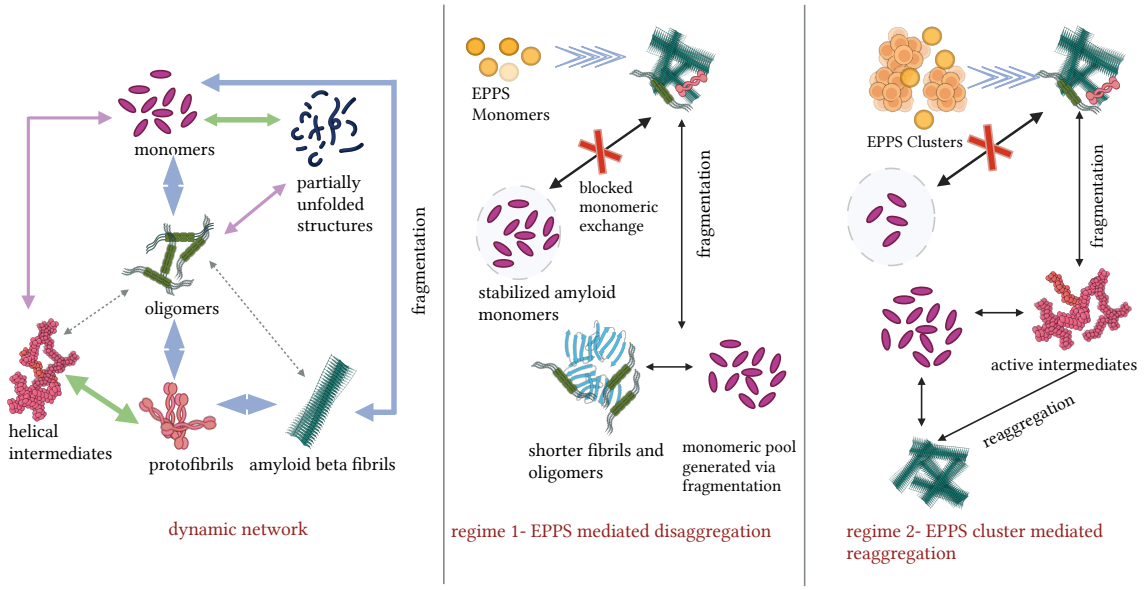

Figure 1: **EPPS-mediated modulation of amyloid assembly**. Initially in the absence of EPPS, fully grown amyloid fibrils exist in dynamic equilibrium with a network of aggregates and monomers (left) . At low concentrations of EPPS (Regime 1), EPPS molecules stabilize amyloid monomers, preventing monomeric exchange which promotes fragmentation of fibrils into shorter fibrils or oligomers generating a new pool of amyloid monomers (middle). At higher EPPS concentrations, EPPS molecules self cluster, reducing the availability of free EPPS monomers to stabilize amyloid monomers. This results in slight fragmentation of amyloid fibrils producing active and unstable intermediates that readily reaggregate due to low free energy barriers (right).

curcumin) [14, 15, 16], Congo red [17], benzofurans [18], and stilbenes [19] have proved promising because they interfere with monomer-monomer interactions. Other approaches that inhibit aggregation employ molecular chaperones [20, 21, 22], metal chelators [23], β-sheet-breaking peptides [24, 25], or monoclonal antibodies [26].

The latter approaches that target preformed aggregates, aiming to restore proteostasis through active disassembly [13], also include several natural products and engineered systems. Prominent examples include (1) flavonols, which remodel amyloids via hydroxyl-mediated disruption of β-sheet stacking [27]; (2) polymeric micelles, which generate reactive oxygen species and promote oxidative fibril cleavage [28]; and (3) molecular chaperones, which drive disassembly through ATP-dependent mechanisms [29], proteolytic fragmentation [30], or isomerase-mediated remodeling [31]. Humanized antibodies such as Crenezumab [32] and Gantenerumab [33] selectively clear aggregated species.

Here, we investigate how EPPS (4-(2-hydroxyethyl)-1-piperazinepropanesulfonic acid), a putative small molecule disaggregase with a molecular weight of 252 Da, reshapes the aggregation landscape of higher order amyloid assemblies. Contrary to the prevailing view that EPPS acts solely through direct and local interactions with amyloid fibrils via its amino sulfonic acid moiety [34, 35, 36], our results indicate that this view does not capture the full mechanism. Instead, the cumulative weight of our experimental evidence, combining optical, fluorescence, vibrational spectroscopic and

electron microscopy data, supports a multiscale hierarchical cooperative mechanism in which higher order mesoscopic assemblies of EPPS interact with amyloid aggregates. In doing so, they control intermolecular interactions at the molecular level and reshape the aggregation landscape, namely the balance between different types of higher order aggregates at the system level. Figure 1 further illustrates the proposed interaction between EPPS and amyloid and its effect on the wider reaction network. Specifically, EPPS and amyloid fibrils, each capable of self-assembly, interact through positive cooperativity, whereby the binding of one EPPS molecule promotes furthur EPPS association with the fibrils. Together, these interactions shift the dynamic balance and reorganize the population of higher order amyloid aggregates across the free-energy landscape. Moreover, our results help explain previous observations of concentration-dependent EPPS behaviour, in which low concentrations promote disaggregation whereas, high concentrations favour aggregation and fibrillation [37]. In addition, they reveal an underappreciated role of molecular crowding in shaping ensemble-level amyloid-drug interactions.

Together, these findings suggest a broader physicochemical principle in amyloid therapeutics: disaggregase efficacy is governed not only by molecular affinity, but by emergent properties arising from self-assembly, cooperativity, and environmental context. EPPS thus serves as a model system for understanding how molecular crowding and dual equilibria regulate amyloid disassembly and reassembly providing insights that may extend to other protein aggregation systems.

Results

EPPS-Aβ Cooperative Interactions

We began by preparing mature Aβ_{42} fibrils, establishing a controlled reference state essential for interpreting perturbations. We aged the fibrils until they reached a steady-state assembly and confirmed this by observing a plateau in Thioflavin T (ThT) fluorescence and by dynamic light scattering (DLS) measurements, which indicated a monodisperse population of stable fibrils (Supplementary Figures S1a, S1b). Subsequently, we assessed how EPPS interacts with Aβ fibrils, producing measurable changes in the balance of aggregation and disassembly.

Alterations in the cross-β structure are expected to be reflected in ThT fluorescence intensity [38], allowing us to monitor the structural changes in real time. ThT kinetics revealed two distinct regimes of EPPS action. At low EPPS concentrations (2-18 μM; Regime 1), fluorescence decreased monotonically, indicating concentration-dependent disassembly of cross-β structures (Figure 2(a)). Fitting the fluoresence intensity traces with a Hill model yielded a half-time (k_D) that decreased, and cooperativity (n_H) that initially increased, with EPPS concentration (Figure 2(b)). These trends indicate that early EPPS-induced perturbations facilitate subsequent molecular engagement, enhancing cooperative destabilization of fibril cores. As EPPS approaches ∼16 μM, this cooperativity declines, marking saturation of accessible binding sites and a transition in mechanism. Hill analysis of the steady-state data (from time-based ThT measurements for Regime 1, Supplementary Figure S2(a)

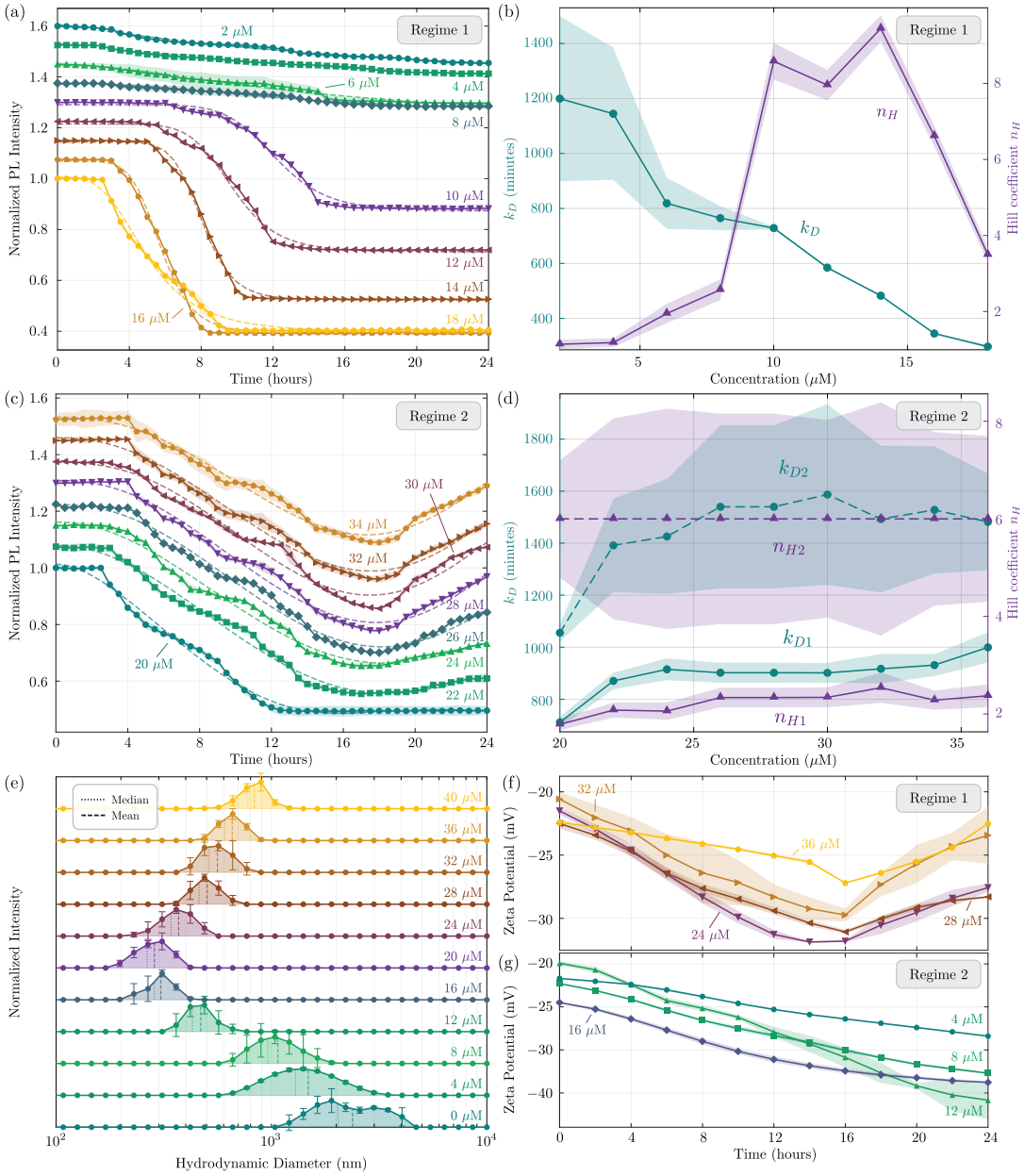

Figure 2: **Kinetics and physicochemical characterization of EPPS treated Aβ**: (a) observed ThT fluorescence intensity as a function of time for lower concentrations of EPPS (2 μM to 18 μM - Regime 1) and (b) corresponding extracted kinetic parameters k_D and n_H extracted using Hill fit. Similarly, (c) ThT fluorescence intensity profiles and (d) kinetic parameters k_{D1}, n_{H1}, k_{D2}, n_{H2} extracted using a double Hill fit for higher EPPS concentrations (20-40 μM, Regime 2). Note, each trace has been vertically displaced in (a) and (c) by 0.075 for clarity. (e) DLS measurements showing changes in amyloid size upon treatment with various concentrations of EPPS; dashed lines indicate the mean, while dotted lines represent the median from three measurements. (f) and (g) show surface charge variations of Aβ during EPPS treatment studied using zeta potential measurements for Regime 1 and Regime 2 respectively. Error bars in (e) and shaded bands (others) represent the standard deviation from three replicate measurements.

and S2(b) and the binding isotherm (Supplementary Figure S3) further support this hypothesis, showing near-complete binding of EPPS close to the transition regime.

At higher concentrations (20-40 μM; Regime 2), the kinetics became biphasic (Figure 2(c)), with an initial disaggregation followed by partial reassembly. We captured these dynamics using a double-Hill model that accounted for two mechanistically linked processes:

$$I(t) = I_0 + \frac{A}{1 + \left(\frac{t}{k_{D1}}\right)^{n_{H1}}} + \frac{B}{1 + \left(\frac{k_{D2}}{t}\right)^{n_{H2}}} \tag{1}$$

where $I(t)$ denotes the measured intensity at time t, I_0 is the initial intensity, k_{D1} and k_{D2} are the half-times, and n_{H1} and n_{H2} are the Hill coefficients for disaggregation and reaggregation, respectively. The first term represents EPPS-induced disassembly, and the second describes delayed reaggregation. Both processes exhibited strong cooperativity, with reaggregation showing higher cooperativity ($n_{H2} > n_{H1} > 1$), indicating that reassembly dominated once intermediates formed (Figure 2(d)). The slower reaggregation rate ($k_{D2} \gg k_{D1}$) and the near-independence of all four parameters on EPPS concentration indicated a self-limiting regime, where disassembly and reassembly proceeded largely according to their intrinsic kinetics rather than being strongly driven by EPPS availability. Together, these results revealed a mechanistic switch from cooperative disassembly at low concentrations to a cyclic disaggregation–reassembly process at higher concentrations, highlighting EPPS as a potent modulator that reshaped the amyloid energy landscape through controlled cooperativity.

Dynamic light scattering (DLS) measurements provided direct physical evidence for the kinetic transitions inferred from the double-Hill analysis. After 24 h of incubation, untreated Aβ_{42} fibrils exhibited a large hydrodynamic size of ~2.4 μm (Figure 2(e)). Upon EPPS addition, the average particle size decreased sharply up to 20 μM, consistent with the concentration-dependent disassembly observed in Regime 1. The mean hydrodynamic size (D_H) dropped from ~2.5 μm to ~ 250 nm, confirming that the rapid loss of ThT intensity reflected the breakdown of large fibrils into smaller, soluble species. At higher concentrations (20–40 μM; Regime 2), the size distribution shifted back toward larger values, with D_H increasing to ~800 nm. This recovery in aggregate size mirrored the k_{D2} reassembly term of the double-Hill kinetics, demonstrating that the high-cooperativity reaggregation in Regime 2 produced new, larger assemblies derived from the fragmented intermediates. The transition from irreversible fragmentation to a dynamic disassembly–reformation cycle was thus quantitatively reflected in the changing hydrodynamic profiles.

Electrostatic measurements further substantiated these kinetic distinctions (Figure 2(f,g)). Zeta potential analysis across EPPS concentrations ranging from 6 to 18 μM revealed a systematic shift toward more negative surface potentials (Figure 2(g)), consistent with increased exposure of negatively charged groups as fibrils disassembled. For example, carboxyl groups likely became more solvent-accessible as cross-β structures fragmented. The progressively more negative charge with rising EPPS concentration supported efficient fibril fragmentation and reinforced the disaggregation-driven mechanism underlying Regime 1.

Beyond 18 μM EPPS, the zeta potential exhibited a biphasic response, paralleling the double-Hill kinetics (Figure 2(f)). Initially, the surface charge became more negative, consistent with the rapid

disaggregation phase (k_{D1}). Over extended incubation, the potential gradually approached neutrality, tracking the slower reassembly event (k_{D2}). The emerging charge compensation likely arose from new intermolecular contacts among fragmented species as they reorganized into higher-order aggregates. Together with ThT and DLS data, these electrostatic measurements established a coherent mechanistic framework: low EPPS concentrations drove cooperative fibril disassembly through charge exposure and size reduction, while higher concentrations triggered a secondary, cooperative reassembly that restored aggregated structure.

To elucidate how small-molecule intervention disrupted the mechanical and structural stability of amyloid, we performed FTIR spectroscopy. FTIR analysis of EPPS-treated amyloid revealed concentration-dependent remodeling of the Aβ backbone, directly capturing how EPPS perturbed the cross-β architecture. Fully matured Aβ_{42} fibrils established a structural reference, with the Amide I region (1600–1700 cm^{-1}) deconvolved using pseudo-Voigt fitting optimized by AIC/BIC analysis [39]. We resolved two principal components: a dominant β-sheet band (1610–1635 cm^{-1}) and a minor contribution from disordered or monomeric segments (1635–1650 cm^{-1}). Quantitative peak-area analysis indicated a β-sheet content of $\sim$80%, defining a rigid baseline for subsequent comparison (Supplementary Figure S4(a)).

Time-resolved FTIR analysis of Aβ_{42} samples treated with 10-40 μM EPPS captured distinct, concentration-dependent transitions in secondary structure (Figure 3(a-d)). A representative figure for the time resolved FTIR measurement is shown in Supplementary Figure S4(b). In Regime 1 (10-20 μM), the spectra exhibited a predictable loss of β-sheet signal within the first 2 h, decreasing from $\sim$78% to $\sim$40%, concurrent with the emergence of a strong α-helical component (Figures 3(a) and (b)). Over extended incubation times (up to 16 h), β-sheet content further declined to $\sim$10%, while the combined α-helix and disordered fractions rose to $\sim$85% . These data confirm that under low EPPS concentrations, fibril disassembly proceeds as a near-complete, time-dependent conversion from ordered β-sheet to non-β conformations, which may include monomeric, oligomeric, or disordered species rather than exclusively fully monomeric forms.

At higher EPPS concentrations, the structural evolution reflected the kinetic complexity of Regime 2. Samples treated with 30 μM EPPS showed an initial collapse of β-sheet content to $\sim$10%, followed by partial recovery to $\sim$35% at longer times, corresponding to the k_{D2} reassembly phase of the double-Hill kinetics (Figure 3(c)). The total disaggregated population peaked at $\sim$90% before declining to $\sim$65%, consistent with partial reformation of higher-order aggregates. At 40 μM, structural profiles exhibited heterogeneous, non-monotonic fluctuations in both β-sheet and disordered fractions, indicative of rapid, simultaneous disaggregation and reassembly and is therefore characteristic of a dynamic, non-equilibrium regime. Overall, EPPS perturbs the fibrillar β-core, with structural outcomes shifting from near-complete disassembly at lower concentrations to reversible, cluster-like reorganization at higher concentrations.

These FTIR observations are consistent with the kinetic and physical measurements. In the first 3-4 hours, FTIR and zeta potential detect early structural and charge shifts, that is loss of β-sheet and increased negative surface potential, before ThT fluorescence changes are observed, suggesting that

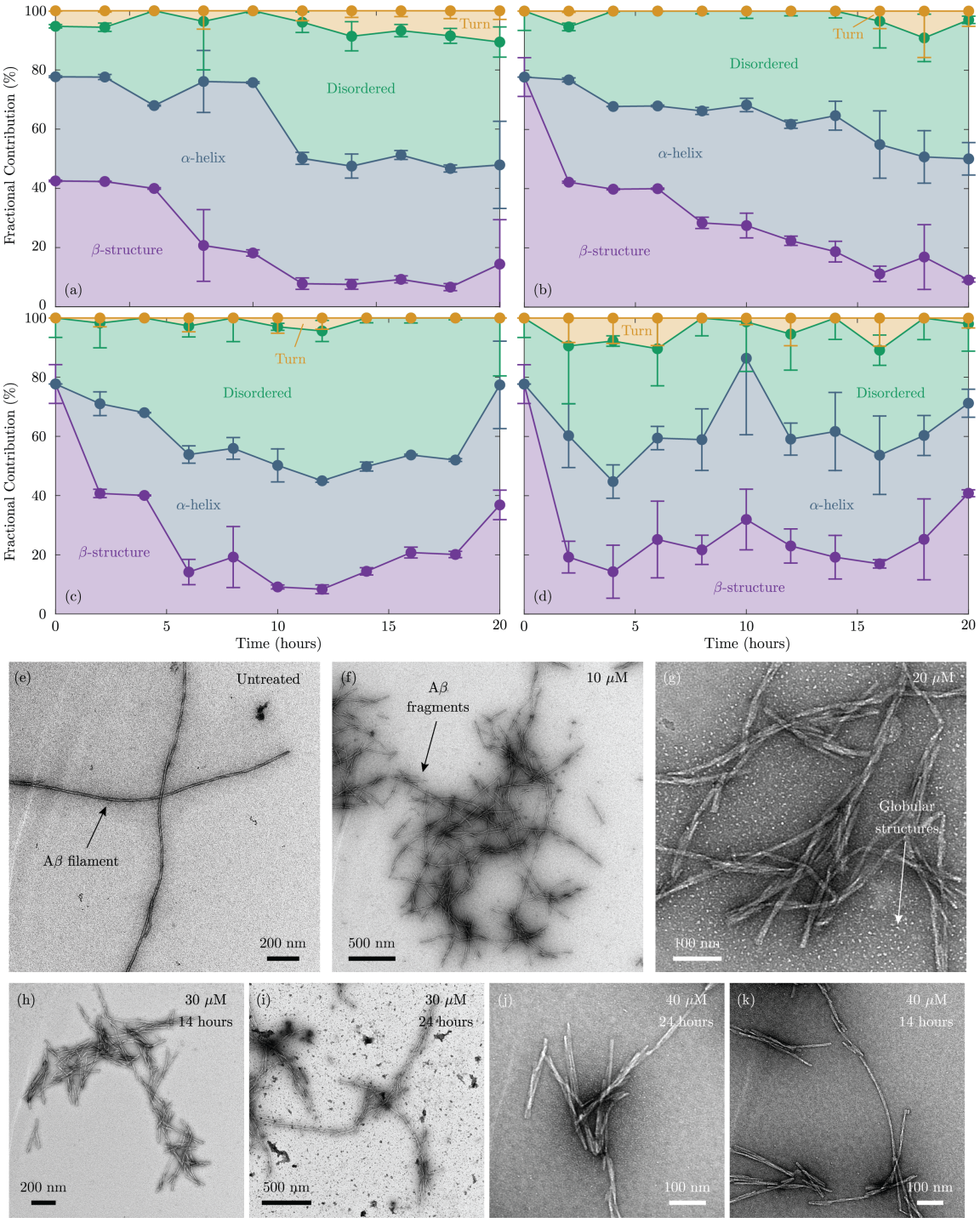

Figure 3: **Structural analysis of EPPS treated Aβ**: (a)-(d): FTIR analysis performed as a function of time for various EPPS concentrations showing structural transitions during disaggregation and reaggregation processes. Stacked plots show fractional contribution of different amyloid secondary structures over time upon treatment with EPPS at (a) 10 μM, (b) 20 μM , (c) 30 μM, and (d) 40 μM. Error bars indicate standard deviation from 3 independent replicates. (e)-(k) : TEM images of (e) untreated Aβ fibril samples, and samples treated with EPPS at (f) 10 μM, (g) 20 μM, (h) 30 μM at 14 h, and (i) 24 h, and 40 μM at (j) 14 h and (k) 24 h.

EPPS initially targets smaller, non-ThT-binding oligomers or protofibrils, promoting α-helical and disordered conformations. The subsequent partial reassembly at intermediate concentrations aligns with DLS-measured size increases and the k_{D2} reassembly term, while high-concentration fluctuations mirror the heterogeneity seen across all probes. Collectively, these results highlight a concentration-dependent, cooperative disaggregation-reassembly mechanism in which EPPS first perturbs early oligomeric structures before modulating larger fibrillar assemblies.

Finally, negative-stain transmission electron microscopy (TEM) provided direct visual confirmation of the morphological transitions inferred from the kinetic and spectroscopic analyses. Untreated Aβ_{42} fibrils appeared as long, unbranched filaments with lengths of ∼1.5-4.5 μm (Figure 3(e)), consistent with a mature, cross-β architecture. Following EPPS treatment, TEM revealed a striking concentration-dependent fragmentation pattern that closely mirrors Regime 1 kinetics. At 10 μM EPPS (Figure 3(f)), fibril lengths were substantially reduced to ∼600-1000 nm, while at 20 μM EPPS (Figure 3(g)), most filaments shortened further to ∼200-500 nm. In addition to these shortened fragments, numerous globular species smaller than ∼10 nm were observed, indicative of extensive breakdown into oligomeric and monomeric intermediates. This concentration (20 μM) corresponds to the point of maximal disaggregation efficiency identified by ThT, DLS, and zeta potential measurements.

Morphological evolution at higher concentrations directly visualized the cooperative reassembly process characteristic of Regime 2. Samples treated with 30 μM EPPS (Figure 3(h)) and 40 μM EPPS (Figure 3(j)) initially displayed pronounced fragmentation after 14 h, with typical lengths of ∼250-500 nm. Prolonged incubation to 24 h led to the emergence of extended fibrillar structures (Figure 3(i) and Figure 3(k)), ranging from ∼800 nm to 2 μm, demonstrating the reappearance of elongated aggregates. This morphological reformation directly parallels the k_{D2}-driven reassembly inferred from the double-Hill kinetics. This trend is corroborated by DLS measurements after 24 h incubation, which show a mean size increase to ∼600 nm at 30 μM to ∼900 nm at 40 μM, as well as the partial β-sheet recovery observed in FTIR.

Longer incubations (4-6 days) produced no further changes in fibril length or morphology relative to the 24 h endpoint, indicating that the EPPS-induced remodeling reaches a stable, dynamic equilibrium between disaggregation and reaggregation. This morphological steady state aligns with the plateau observed in ThT and DLS profiles, underscoring the self-limiting nature of EPPS action (Supplementary Figures S5(a-h)).

The incomplete disaggregation and self-limiting steady state observed at higher EPPS concentrations could not be explained based on the observed fibril structure, as both Regime 1 and Regime 2 ultimately yielded similar non-β-sheet end products. This suggested that the availability of active EPPS monomers might be reduced at elevated concentrations, prompting us to hypothesize that dynamic EPPS self-association, driven by its zwitterionic framework, sequesters monomers into transient clusters and thereby limits their accessibility for fibril binding.

Dynamic light scattering (DLS) measurements directly supported this mechanism (Figure 4). Below 20 μM, EPPS existed as monomeric or weakly associated species with hydrodynamic radii under

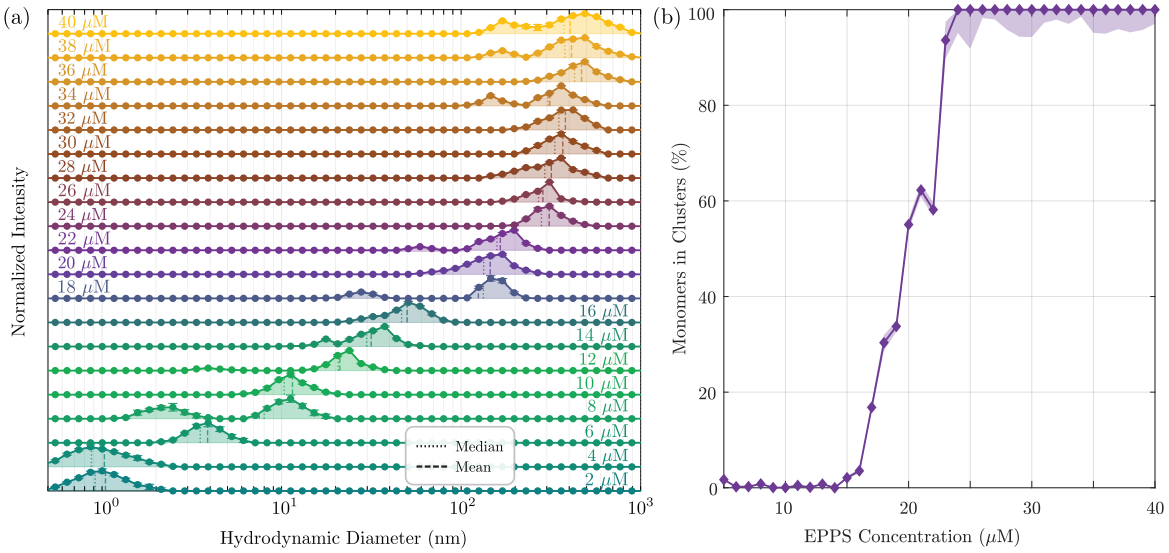

Figure 4: **EPPS clustering dynamics as a function of concentration**: (a) DLS measurements of EPPS clustering after 24 h incubation across a range of concentrations from 2 to 40 μM. At low EPPS concentrations (2-10 μM), the clusters remain very small, with average sizes below 10 nm, close to the monomeric state. As the concentration increases beyond 10 μM, larger clusters begin to form, reaching sizes of 600-800 nm at the highest EPPS concentrations. The corresponding DLS spectra are presented, with each trace vertically offset for clarity. Dashed and dotted lines indicate the mean and median cluster sizes, respectively, and error bars represent the standard deviation from three independent replicates. (b) Percentage of EPPS incorporated into clusters as a function of EPPS concentration, extracted from DLS intensity distributions after conversion to number distributions using Rayleigh - Mie scattering models. The fraction of EPPS incorporated into clusters remains nearly zero below ~15 μM, beyond which it rises sharply, reaching close to 100% around ~25 μM. This concentration-dependent transition aligns closely with the regimes defined earlier.

100 nm. Above this threshold, a sharp transition occurred, with sizes increasing to ~400-500 nm at 30-40 μM, consistent with extensive self-association. To quantify the relative populations of freely diffusing monomers and clustered species, DLS intensity distributions were converted into approximate number distributions using established scattering theory. Size-dependent scattering effects were treated using a Rayleigh-Mie framework, with the Mie theory applied to clusters larger than 60 nm to account for Mie scattering contributions. This analysis reveals that EPPS remains predominantly monomeric at concentrations below 15μM, whereas the clustered species become the dominant population above 25 μM (Figure 4(b)). Notably, this corresponds to a marked depletion of freely diffusible monomers within the concentration window defining the transition between Regime 1 and Regime 2 , indicating a concentration-driven redistribution of EPPS from monomeric to ensemble level clustered states. More details on the calculation are provided in Supplementary Section 6. Under high-salt conditions (200 mM NaCl), DLS recorded substantially larger particle sizes at each concentration, confirming that EPPS forms electrostatically stabilized dynamic clusters that reorganize upon ionic

screening (Supplementary Figure S6).

To summarise, the results presented in this section provide a mechanistic basis for the diminished disaggregation efficiency observed at high EPPS concentrations. Clustering reduces the pool of active monomers, leading to incomplete fibril disruption and promoting partial reassembly of fragmented species. Complementary ThT assays showed that, once disaggregation reached a plateau, it persisted for 5-6 h without fluorescence recovery, indicating the formation of off-pathway, non-propagating intermediates. At still higher concentrations, reduced EPPS bioavailability permits a subset of these intermediates to re-enter aggregation-competent pathways, restoring cross-β order over time.

Kinetic analysis reinforces this interpretation. In Regime 2, the apparent disaggregation rate constant (k_{D1}) decreased markedly relative to Regime 1, consistent with limited monomer accessibility. Concurrently, the reaggregation rate constant (k_{D2}) increased before reaching a plateau, indicating that self-association constrains both disassembly and reassembly kinetics. The Hill coefficient for disaggregation (n_{H1}) rose modestly yet remained below Regime 1 values, implying that although fewer monomers are available, those remaining act cooperatively at fibril surfaces. In contrast, the Hill coefficient for reaggregation (n_{H2}) remained constant, suggesting a diffusion-limited mechanism involving intermediate species rather than concerted cooperative events. Similar behavior was observed for the zwitterionic compound HEPES, which is structurally analogous to EPPS but differs in the length of its hydrocarbon chain. HEPES exhibited a comparable two-regime behavior, though with a shifted transition threshold (Supplementary Figure S7(a-d)). DLS (Supplementary Figure S7(e)) confirmed that HEPES also undergoes concentration-dependent clustering, forming transient assemblies akin to those of EPPS. These parallels reveal a broader principle: small-molecule modulators regulate amyloid network dynamics through concentration-dependent coupling of monomer availability, self-association, and fibril surface engagement. At optimal concentrations, these molecules drive cooperative disassembly into off-pathway, disordered species, whereas at higher loadings, dynamic self-association limits their bioactivity, yielding a self-regulated equilibrium between disaggregation and reassembly.

Interactions of Aβ and EPPS in macromolecularly crowded environments

Cellular environments impose macromolecular crowding that can constrain fibril dynamics. To investigate how such conditions modulate EPPS activity, we incubated mature Aβ_{42} fibrils with PEG2000, a crowding agent that promotes volume exclusion and stabilizes compact fibril networks [40]. TEM imaging of PEG-crowded fibrils revealed pronounced morphological remodeling relative to uncrowded controls (Figure 5(a,b)). Previously straight filaments became shorter, bent, and interconnected, forming network-like arrangements. Network domains varied, with the largest spanning 3-4 μm, alongside smaller clusters of 300-1000 nm. In several regions, the fibrils looped or formed partial rings, indicating enhanced lateral association and flexibility under steric constraints. PEG-induced crowding thus promotes fibril bending, lateral interactions, and network formation, producing a more interconnected amyloid architecture.

Treatment with 20 μM EPPS for 24 h largely disrupted large network domains (Figure 5(c,d)),

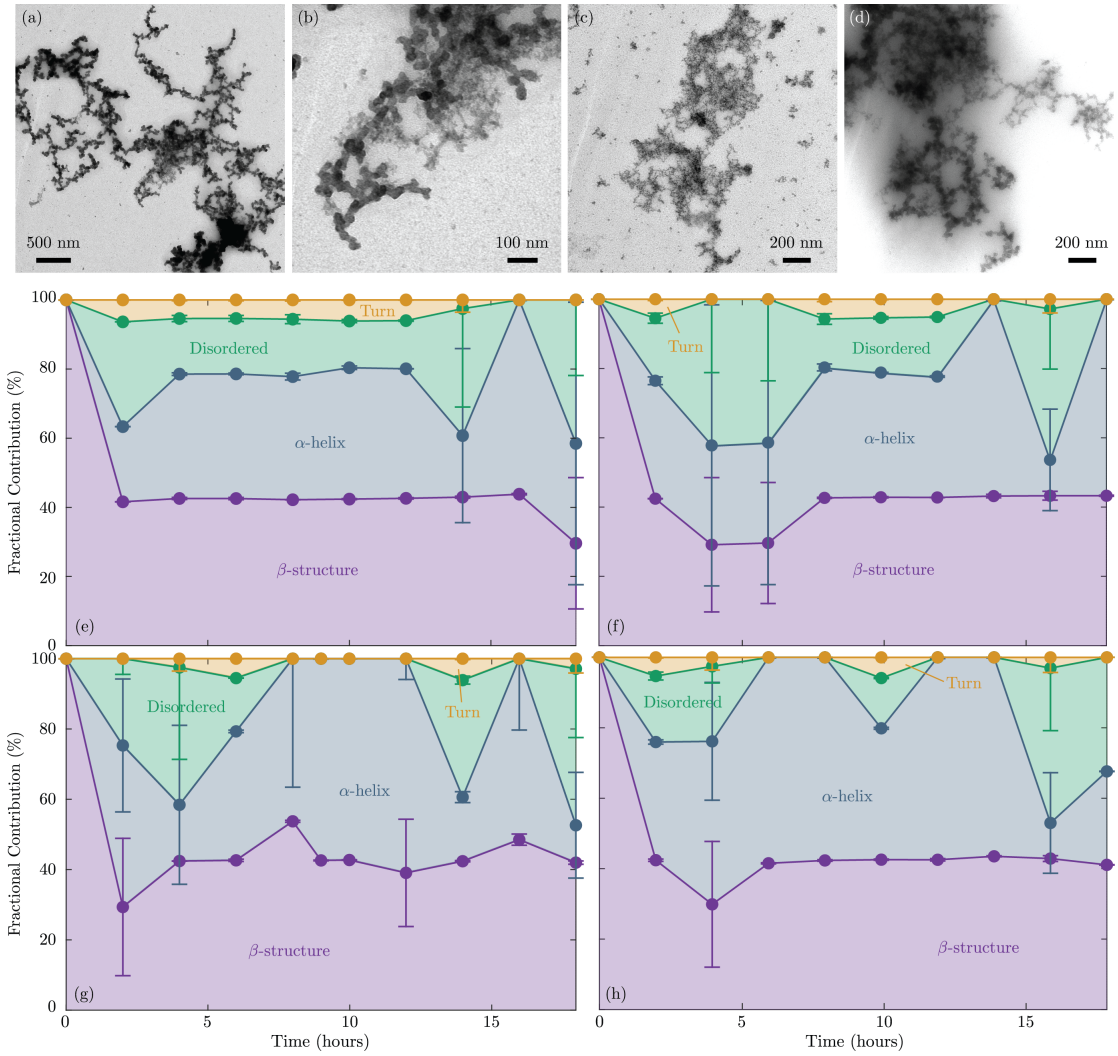

Figure 5: **Effect of macromolecular crowding on EPPS induced restructuring of amyloid**: (a) and (b) TEM images of PEG-crowded Aβ fibrils. (c) and (d) TEM images of PEG crowded Aβ fibrils after treatment with 20 μM EPPS for 24 h. (e)-(h) FTIR-derived fractional contributions of secondary structural components as a function of time after treatment with EPPS concentrations of (e) 10 μM, (f) 20 μM, (g) 30 μM and (h) 40 μM. Error bars in panels (e)-(h) represent the standard deviation of fractional contributions obtained from three independent replicates.

generating heterogeneous smaller clusters of ∼200-800 nm while individual fibrils retained elongated morphology. TEM images for treatments with other concentrations of EPPS are shown in Supplementary Figures S8(a-f). These observations suggest that EPPS primarily remodels inter-fibrillar contacts, converting large aggregates into smaller assemblies while preserving the intra-fibrillar cross-β core. DLS measurements confirmed pronounced size heterogeneity under crowding (Supplementary Figure S9), indicating that although EPPS remodels large clusters, crowding limits complete fibril disassembly.

ThT fluorescence of PEG-crowded fibrils treated with 2-40 μM EPPS exhibited irregular fluctuations similar to PEG-only controls (Supplementary Figure S10), reflecting aggregate-size hetero-

geneity. The mean ThT signal remained largely unchanged, indicating that individual fibril cross-β architecture persisted despite partial network remodeling. These results suggest that EPPS efficacy depends on solvent-exposed β-sheet regions, which may be sterically shielded under crowded conditions.

FTIR spectroscopy further provided molecular resolution of these structural changes. The deconvolved Amide I spectrum of PEG-treated controls indicated complete β-sheet content (Supplementary Figure S11(a)), consistent with fibril stabilization. EPPS treatment (10-40 μM) induced a rapid reduction of β-sheet signal to $\sim$42% within the first 2 h, accompanied by transient α-helical features (Figures 5(e-h)). A representative figure of the FTIR spectrum at a given time is shown in Supplementary Figure S11(b)). The disordered fraction fluctuated without a clear concentration trend, and no further evolution was observed up to 18 h. Measurements taken at 20 min intervals during the first 2 h revealed that β-sheet content collapsed almost entirely within 20 min, concurrent with a surge in α-helical signal, after which the secondary structure distribution stabilized (Supplementary Figure S12(a-d)). Fluctuations in the disordered fraction likely reflect transient intermediate states formed during early disassembly.

These data define two structurally distinct populations. A labile subset ($\sim$58%), comprising protofibrils or oligomers retaining β-sheet character, undergoes rapid EPPS-induced disassembly even under crowded conditions. The remaining $\sim$42% represents PEG-stabilized fibrils whose cross-β cores resist EPPS action due to steric shielding. Consistent with ThT data, the fibrillar core remains largely intact, while partial relaxation occurs in exposed regions detectable by FTIR.

Overall, PEG-induced crowding enforces a biphasic disaggregation response: a rapid loss of accessible β-sheet regions followed by stabilization of protected fibrillar domains. This confinement-driven protection highlights how cellular crowding can fundamentally constrain the efficiency of small-molecule disaggregases such as EPPS, limiting their access to structured fibril cores.

Complementary ThT and FTIR analyses together provide a coherent view of EPPS activity under crowded conditions. Although ThT fluorescence remained largely unchanged, FTIR revealed a rapid loss of β-sheet content accompanied by the emergence of α-helical structures, indicating that EPPS primarily perturbs inter-fibrillar β-contacts without fully disrupting the cross-β cores. These molecular changes align with TEM observations showing the conversion of large amyloid networks into smaller, partially ordered clusters. Under PEG-induced crowding, densely packed fibrils embed their rigid cross-β domains within compact assemblies, sterically limiting EPPS access, whereas peripheral fibrils remain more exposed and responsive.

Collectively, these findings reveal that the disassembly of amyloid networks by EPPS is governed by both the dynamic organization of EPPS molecules and the physicochemical microenvironment. Even in uncrowded conditions, EPPS forms transient clusters, and under confinement these self-associating species engage amyloid collectively rather than as individual monomers. This framework establishes that a small molecule's efficacy depends not only on its chemical identity but also on its dynamic assembly state and local environment, highlighting how molecular clustering can finely tune the balance between amyloid stability and disassembly.

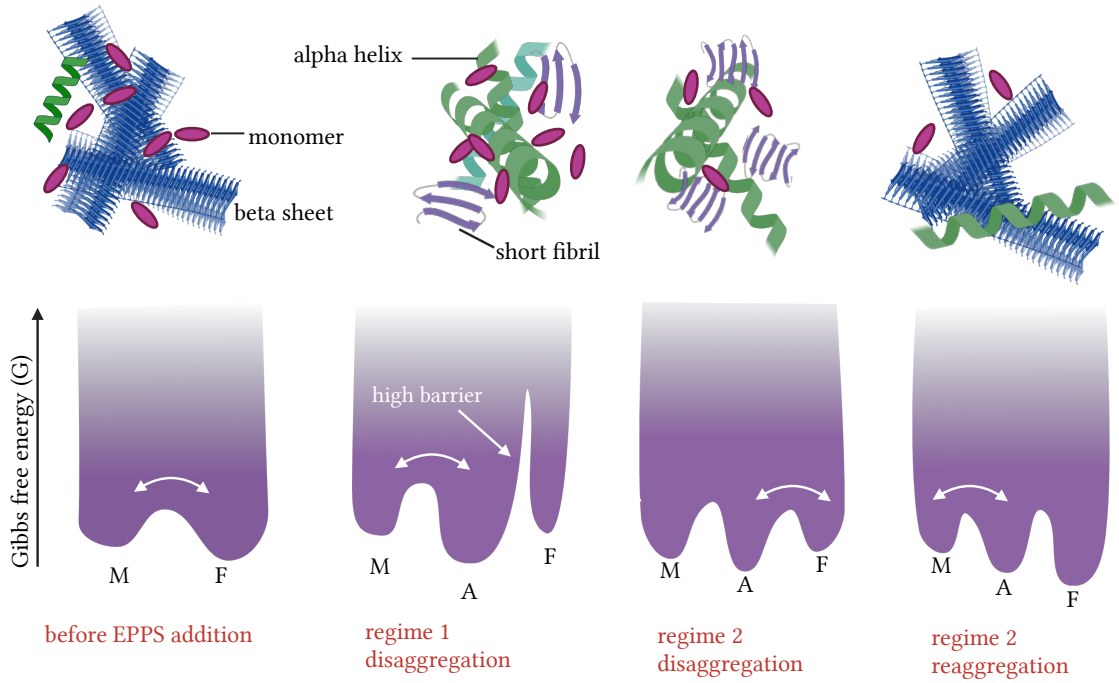

lower order aggregate (M), active intermediates (A), higher order fibrillar species (F)

Figure 6: **Proposed aggregation landscape model for EPPS-mediated Aβ disaggregation and reorganization**: (top row) Schematic illustration of distinct EPPS-Aβ interaction regimes as a function of EPPS concentration. At low EPPS concentrations (Regime 1), EPPS interacts with preformed Aβ fibrils and promotes disaggregation, leading to fibril fragmentation and the release of smaller species, including monomers and α-like conformations. In this regime, disaggregation dominates and the system shifts away from mature fibrillar assemblies. At higher EPPS concentrations (Regime 2), EPPS clustering further enhances fibril destabilization; however, the increased local concentration of released Aβ species facilitates partial re-aggregation, giving rise to a competing pathway alongside continued disaggregation. (bottom row) Schematic representation of the aggregation landscape describing Aβ assembly in the presence of EPPS. In the absence of perturbation, various amyloid species coexist in a dynamic equilibrium, populating two interconnected funnels corresponding to lower-order aggregates and mature fibrillar assemblies. EPPS is hypothesized to stabilize the lower-order population, thereby reshaping the aggregation landscape, shifting the equilibrium away from deep fibrillar minima, and lowering the energetic barrier for fibril disassembly while retaining a shallow minimum that permits partial re-aggregation of released fragments.

Discussion

The concentration-dependent disaggregation, self-association, and biphasic kinetics observed across our experiments prompted us to investigate the mechanistic origin of these behaviours (schematic in top row of Figure 6). While direct binding of EPPS to fibril surfaces (as proposed by several groups)

may contribute to fibril destabilization, several features of our data indicate that this mechanism alone is insufficient. In particular, the near-stoichiometric EPPS:Aβ ratios required for activity, the strong correspondence between EPPS clustering and kinetic regime transitions, and the early emergence of α-helical intermediates all point to a more nuanced mode of action.

Given the well-established capacity of zwitterionic molecules to stabilize lower-order protein species, we propose that EPPS additionally acts through an equilibrium-shift mechanism (bottom row of Figure 6). Under native conditions, the aggregation landscape is dominated by two principal wells corresponding to lower-order aggregates (M)—including monomers and small oligomers—and mature β-sheet-rich fibrillar structures (F), consistent with our FTIR-derived population ratio of approximately 20% disordered/lower-order species and 80% β-sheet-rich fibrils. We further introduce an intermediate active state (A), comprising α-helical or structurally labile conformations that dynamically participate in the aggregation-disaggregation pathway. By virtue of its zwitterionic character, EPPS may lower the free energy of the lower-order species and stabilize the active α-structured intermediates, while increasing the activation barrier associated with β-sheet nucleation. This redistribution perturbs the fibril-lower-order equilibrium, driving compensatory fibril fragmentation to restore the native balance. This mechanism is distinct from classical ligand-induced mechanical disaggregation and instead reflects an equilibrium-driven redistribution of conformational populations.

This framework provides a coherent explanation for the two concentration-dependent regimes observed experimentally:

Regime 1 (low EPPS concentration): Lower-order aggregate stabilization dominates, lowering the free energy of the M basin and promoting progressive disassembly of mature fibrils (F). Once the system approaches the new equilibrium, the barrier separating the active intermediates (A) from the fibril well remains sufficiently high that further transitions are kinetically suppressed. As a result, partially folded or disordered lower-order species accumulate in local minima, producing the plateaued disaggregation behavior captured in Figure 6 (bottom row, second panel).

Regime 2 (high EPPS concentration): At elevated EPPS concentrations, dynamic clustering reduces the pool of freely available EPPS molecules. This limits the extent to which EPPS can deepen the lower-order aggregate (M) basin or raise the β-sheet nucleation barrier for fibrils (F). Consequently, after an initial period of M stabilization and rapid F fragmentation (Figure 6, bottom row third panel), the barrier separating M and F states remains comparatively low. Under these conditions, trapped active intermediates (A) and other lower-order species can re-enter the fibril basin over experimentally relevant timescales (Figure 6 bottom row fourth panel). Their return increases the local M population within the F well, driving time-dependent reaggregation as the system attempts to re-attain equilibrium. This reversible flow between free-energy wells accounts for the biphasic behavior observed in our kinetics, FTIR spectra, and morphological analyses.

Taken together, these findings suggest that EPPS functions as an aggregation landscape modulator whose efficacy depends on its concentration, assembly state, and ability to reshape the free energy

landscape governing Aβ folding and aggregation. By tuning both the depth of the monomeric basin and the height of the β-sheet conversion barrier, EPPS dictates whether the system resides in a disassembly-dominant or reassembly-permissive regime.

Methods

Amyloid fibril preparation

Amyloid beta 42 (Aβ) was purchased from Abcam. Lyophilized amyloid powder (1 mg) was stored at -80°C. To prepare amyloid fibrils, peptide aliquot was dissolved in 10mM NaOH and immediately diluted with phosphate buffered saline (PBS, pH 7.2) to reach 20 μM Aβ solution. The resulting solution was incubated at 37°C with gentle agitation for 24-36 hours to allow the formation of fibrils. Fibril formation was further confirmed using Thioflavin T fluorescence assays and TEM imaging.

Preparation of EPPS-Amyloid assay

EPPS solutions were prepared by dissolving EPPS in deionized water (pH 6.5) and immediately used. Fully grown amyloid fibrils were mixed with EPPS solution to obtain final EPPS concentrations ranging from 2 μM to 40 μM (step size 2 μM). The final mixtures of EPPS and amyloid had a pH of around 6.8. These mixtures were then subsequently used for spectroscopic measurements and imaging analyses.

PEG crowded amyloid assay

Cell-mimicking crowded assays were prepared by adding the crowding molecule PEG-2000 (50% w/v) to a 20 μM Aβ fibril solution. PEG:amyloid ratios were varied from 1:10 to 1:2. The mixtures were incubated for 24 hours prior to measurements. The resulting samples were used for spectroscopic measurements and imaging analyses to monitor size changes in amyloid aggregates.

Fluorescence measurements

Amyloid aggregation was monitored using the Thioflavin T (ThT) fluorescence assay. For the assay, a 20 μM Aβ solution was mixed with 10 μM ThT solution. Three independent samples were prepared, and 50 μL of each was loaded into a microwell plate for fluorescence measurements. Measurements were carried out using a SpectraMax iD5 multimode microwell plate reader (Molecular Devices) with a spectral resolution of 1 nm. The excitation wavelength was 440 nm, and emission was monitored at 485 nm. The experiment was conducted continuously for 24 hours and the readings were taken at 30 minute intervals. Before each reading, the plate was shaken gently for 5 seconds to ensure uniform mixing.

DLS studies

DLS measurements were performed using Zetasizer advanced ultra (Malvern Panalytical) at 25°C in low volume disposable plastic cuvettes with a 500 μl sample volume. The instrument provides particle resolution of approximately 2:1, capable of distinguising particle populations differing by two fold size. DLS was used to monitor size changes during amyloid growth, EPPS-induced amyloid disaggregation and reaggregation as well as EPPS self-clustering. Measurements were collected over 25 cycles, and the samples were measured 3 to 4 times and averaged to get the mean size distribution. Three independent replicates were analysed for all samples following the same procedure.

FTIR Measurements

FTIR measurements were performed using a Shimadzu IRTracer-100 to obtain structural information on amyloid intermediates and secondary structures formed during EPPS interactions in both buffer and crowded environments. Experiments were conducted at a spectral resolution of 2 cm^{-1} with 256-scan averaging. Background spectra of the corresponding buffer were subtracted prior to each measurement to ensure accurate analysis. Samples ($\sim$2 μL) were measured in attenuated total reflectance (ATR) mode by directly applying the solution onto the diamond crystal at room temperature. Three independent replicates were performed for each condition.

Zeta potential studies

Zeta potential measurements were carried out using a Zetasizer Advanced Ultra (Malvern Panalytical) at 25°C in low-volume disposable cuvettes with an applied voltage across the electrodes. Samples were prepared in phosphate-buffered saline (PBS, pH 7.4) and equilibrated for 30 s before measurement. For each sample, three measurements were taken and averaged, and three independent replicates were performed. Measurements were used to monitor changes in the surface charge of amyloid fibrils during EPPS-induced disaggregation and reaggregation.

Transmission Electron Microscopy

For negative stain TEM, 5 μL of each sample was incubated for 60 s on a freshly glow discharged copper grid covered with a continuous carbon film. The grids were blotted with a filter paper and stained by applying a drop of 1% uranyl acetate on grids for 60 s, blotted with filter paper and air-dried for 10 min before TEM viewing. The grids were imaged using FEI Tecnai 120 keV with a digital CCD Eagle camera 4k $\times$ 4k (Thermo Fisher Scientific,USA).

Acknowledgments

This research is supported by the Ministry of Education, Singapore, under its Research Centre of Excellence award to the Institute for Digital Molecular Analytics & Science, NTU (IDMxS, grant:

EDUNC-33-18-279-V12). The authors acknowledge the use of NISB Cryogenic Electron Microscopy Platform at NTU Institute of Structural Biology (NISB), Nanyang Technological University.

References

[1] Mikio Shoji, Todd E Golde, Jorge Ghiso, Tobun T Cheung, Steven Estus, Lillian M Shaffer, Xiao-Dan Cai, Deborah M McKay, Ron Tintner, Bias Frangione, et al. Production of the alzheimer amyloid β protein by normal proteolytic processing. *Science*, 258(5079):126–129, 1992.

[2] Colin J Barrow and Michael G Zagorski. Solution structures of β peptide and its constituent fragments: relation to amyloid deposition. *Science*, 253(5016):179–182, 1991.

[3] Massimo Stefani and Christopher M Dobson. Protein aggregation and aggregate toxicity: new insights into protein folding, misfolding diseases and biological evolution. *Journal of molecular medicine*, 81(11):678–699, 2003.

[4] Sandra Chimon, Medhat A Shaibat, Christopher R Jones, Diana C Calero, Buzulagu Aizezi, and Yoshitaka Ishii. Evidence of fibril-like β-sheet structures in a neurotoxic amyloid intermediate of alzheimer's β-amyloid. *Nature structural & molecular biology*, 14(12):1157–1164, 2007.

[5] Mahiuddin Ahmed, Judianne Davis, Darryl Aucoin, Takeshi Sato, Shivani Ahuja, Saburo Aimoto, James I Elliott, William E Van Nostrand, and Steven O Smith. Structural conversion of neurotoxic amyloid-β1–42 oligomers to fibrils. *Nature structural & molecular biology*, 17(5):561–567, 2010.

[6] Li-Quan Yang, Xing-Lai Ji, and Shu-Qun Liu. The free energy landscape of protein folding and dynamics: a global view. *Journal of Biomolecular Structure and Dynamics*, 31(9):982–992, 2013.

[7] Weihua Zheng, Min-Yeh Tsai, Mingchen Chen, and Peter G Wolynes. Exploring the aggregation free energy landscape of the amyloid-β protein (1–40). *Proceedings of the National Academy of Sciences*, 113(42):11835–11840, 2016.

[8] Tuomas P. J. Knowles, Christopher A. Waudby, Glyn L. Devlin, Samuel I. A. Cohen, Adriano Aguzzi, Michele Vendruscolo, Eugene M. Terentjev, Mark E. Welland, and Christopher M. Dobson. An analytical solution to the kinetics of breakable filament assembly. *Science*, 326(5959):1533–1537, 2009.

[9] Samuel IA Cohen, Sara Linse, Leila M Luheshi, Erik Hellstrand, Duncan A White, Luke Rajah, Daniel E Otzen, Michele Vendruscolo, Christopher M Dobson, and Tuomas PJ Knowles. Proliferation of amyloid-β42 aggregates occurs through a secondary nucleation mechanism. *Proceedings of the National Academy of Sciences*, 110(24):9758–9763, 2013.

[10] Mathias Jucker and Lary C Walker. Propagation and spread of pathogenic protein assemblies in neurodegenerative diseases. *Nature neuroscience*, 21(10):1341–1349, 2018.

[11] Yun Zhang, Huaqiu Chen, Ran Li, Keenan Sterling, and Weihong Song. Amyloid β-based therapy for alzheimer's disease: challenges, successes and future. *Signal transduction and targeted therapy*, 8(1):248, 2023.

[12] Torleif Härd and Christofer Lendel. Inhibition of amyloid formation. *Journal of molecular biology*, 421(4-5):441–465, 2012.

[13] Kimberly Jia Yi Low, Anandalakshmi Venkatraman, Jodhbir S Mehta, and Konstantin Pervushin. Molecular mechanisms of amyloid disaggregation. *Journal of Advanced Research*, 36:113–132, 2022.

[14] Yin-Lei Han, Huan-Huan Yin, Chao Xiao, Matthew T Bernards, Yi He, and Yi-Xin Guan. Understanding the molecular mechanisms of polyphenol inhibition of amyloid β aggregation. *ACS Chemical Neuroscience*, 14(22):4051–4061, 2023.

[15] Luiza Fernandes, Thyago R Cardim-Pires, Debora Foguel, and Fernando L Palhano. Green tea polyphenol epigallocatechin-gallate in amyloid aggregation and neurodegenerative diseases. *Frontiers in neuroscience*, 15:718188, 2021.

[16] Arjun Thapa, Stephen D Jett, and Eva Y Chi. Curcumin attenuates amyloid-β aggregate toxicity and modulates amyloid-β aggregation pathway. *ACS chemical neuroscience*, 7(1):56–68, 2016.

[17] Alfredo Lorenzo and Bruce A Yankner. Beta-amyloid neurotoxicity requires fibril formation and is inhibited by congo red. *Proceedings of the National Academy of Sciences*, 91(25):12243–12247, 1994.

[18] Stefano Rizzo, Céline Rivière, Lorna Piazzi, Alessandra Bisi, Silvia Gobbi, Manuela Bartolini, Vincenza Andrisano, Fabiana Morroni, Andrea Tarozzi, Jean-Pierre Monti, et al. Benzofuran-based hybrid compounds for the inhibition of cholinesterase activity, β amyloid aggregation, and aβ neurotoxicity. *Journal of medicinal chemistry*, 51(10):2883–2886, 2008.

[19] Céline Rivière, Tristan Richard, Lysiane Quentin, Stéphanie Krisa, Jean-Michel Mérillon, and Jean-Pierre Monti. Inhibitory activity of stilbenes on alzheimer's β-amyloid fibrils in vitro. *Bioorganic & medicinal chemistry*, 15(2):1160–1167, 2007.

[20] Christopher G Evans, Susanne Wisén, and Jason E Gestwicki. Heat shock proteins 70 and 90 inhibit early stages of amyloid β-(1–42) aggregation in vitro. *Journal of Biological Chemistry*, 281(44):33182–33191, 2006.

[21] Ana Rodríguez-Ramos, Jesús A González, and Mónica L Fanarraga. Enhanced inhibition of amyloid formation by heat shock protein 90 immobilized on nanoparticles. *ACS Chemical Neuroscience*, 14(15):2811–2817, 2023.

[22] Patricia Yuste-Checa, Alonso I Carvajal, Chenchen Mi, Sarah Paatz, F Ulrich Hartl, and Andreas Bracher. Structural analyses define the molecular basis of clusterin chaperone function. *Nature Structural & Molecular Biology*, pages 1–11, 2025.

[23] Ling Huang, Chuanjun Lu, Yang Sun, Fei Mao, Zonghua Luo, Tao Su, Huailei Jiang, Wenjun Shan, and Xingshu Li. Multitarget-directed benzylideneindanone derivatives: anti-β-amyloid (aβ) aggregation, antioxidant, metal chelation, and monoamine oxidase b (mao-b) inhibition properties against alzheimer's disease. *Journal of medicinal chemistry*, 55(19):8483–8492, 2012.

[24] Vinod Jani, Uddhavesh Sonavane, and Rajendra Joshi. Destabilization potential of beta sheet breaker peptides on abeta fibril structure: an insight from molecular dynamics simulation study. *RSC advances*, 11(38):23557–23573, 2021.

[25] Yang Song, Edwin G Moore, Yanshu Guo, and Jeffrey S Moore. Polymer–peptide conjugates disassemble amyloid β fibrils in a molecular-weight dependent manner. *Journal of the American Chemical Society*, 139(12):4298–4301, 2017.

[26] Beka Solomon, Rela Koppel, Eilat Hanan, and Tamar Katzav. Monoclonal antibodies inhibit in vitro fibrillar aggregation of the alzheimer beta-amyloid peptide. *Proceedings of the National Academy of Sciences*, 93(1):452–455, 1996.

[27] Kentaro Noi, Kensuke Ikenaka, Hideki Mochizuki, Yuji Goto, and Hirotsugu Ogi. Disaggregation behavior of amyloid β fibrils by anthocyanins studied by total-internal-reflection-fluorescence microscopy coupled with a wireless quartz-crystal microbalance biosensor. *Analytical Chemistry*, 93(32):11176–11183, 2021.

[28] Hao Geng, Hongbo Yuan, Liang Qiu, Dong Gao, Yongqiang Cheng, and Chengfen Xing. Inhibition and disaggregation of amyloid β protein fibrils through conjugated polymer–core thermoresponsive micelles. *Journal of Materials Chemistry B*, 8(44):10126–10135, 2020.

[29] Ricarda Törner, Tatsiana Kupreichyk, Wolfgang Hoyer, and Jerome Boisbouvier. The role of heat shock proteins in preventing amyloid toxicity. *Frontiers in molecular biosciences*, 9:1045616, 2022.

[30] Sheng Chen, Anuradhika Puri, Braxton Bell, Joseph Fritsche, Hector H Palacios, Maurie Balch, Macy L Sprunger, Matthew K Howard, Jeremy J Ryan, Jessica N Haines, et al. Htra1 disaggregates α-synuclein amyloid fibrils and converts them into non-toxic and seeding incompetent species. *Nature communications*, 15(1):2436, 2024.

[31] Jeremy D Baker, Lindsey B Shelton, Dali Zheng, Filippo Favretto, Bryce A Nordhues, April Darling, Leia E Sullivan, Zheying Sun, Parth K Solanki, Mackenzie D Martin, et al. Human cyclophilin 40 unravels neurotoxic amyloids. *PLoS biology*, 15(6):e2001336, 2017.

[32] Mark Ultsch, Bing Li, Till Maurer, Mary Mathieu, Oskar Adolfsson, Andreas Muhs, Andrea Pfeifer, Maria Pihlgren, Travis W Bainbridge, Mike Reichelt, et al. Structure of crenezumab complex with aβ shows loss of β-hairpin. *Scientific reports*, 6(1):39374, 2016.

[33] Bernd Bohrmann, Karlheinz Baumann, Jörg Benz, Francoise Gerber, Walter Huber, Frédéric Knoflach, Jürg Messer, Krisztina Oroszlan, Robert Rauchenberger, Wolfgang F Richter, et al.

Gantenerumab: a novel human anti-aβ antibody demonstrates sustained cerebral amyloid-β binding and elicits cell-mediated removal of human amyloid-β. *Journal of Alzheimer's Disease*, 28(1):49–69, 2012.

[34] Hye Yun Kim, Hyunjin Vincent Kim, Seonmi Jo, C Justin Lee, Seon Young Choi, Dong Jin Kim, and YoungSoo Kim. Epps rescues hippocampus-dependent cognitive deficits in app/ps1 mice by disaggregation of amyloid-β oligomers and plaques. *Nature communications*, 6(1):8997, 2015.

[35] YoungSoo Kim, Yong Kyoung Yoo, Hye Yun Kim, Jee Hoon Roh, Jinsik Kim, Seungyeop Baek, Jinny Claire Lee, Hye Jin Kim, Myung-Sic Chae, Dahye Jeong, et al. Comparative analyses of plasma amyloid-β levels in heterogeneous and monomerized states by interdigitated microelectrode sensor system. *Science advances*, 5(4):eaav1388, 2019.

[36] Kevin A Murray, Carolyn J Hu, Hope Pan, Jiahui Lu, Romany Abskharon, Jeannette T Bowler, Gregory M Rosenberg, Christopher K Williams, Gazmend Elezi, Melinda Balbirnie, et al. Small molecules disaggregate alpha-synuclein and prevent seeding from patient brain-derived fibrils. *Proceedings of the National Academy of Sciences*, 120(7):e2217835120, 2023.

[37] Wonseok Lee, Sang Won Lee, Gyudo Lee, and Dae Sung Yoon. Atomic force microscopy analysis of epps-driven degradation and reformation of amyloid-β aggregates. *Journal of Alzheimer's disease reports*, 2(1):41–49, 2018.

[38] Matthew Biancalana, Koki Makabe, Akiko Koide, and Shohei Koide. Molecular mechanism of thioflavin-t binding to the surface of β-rich peptide self-assemblies. *Journal of Molecular Biology*, 385(4):1052–1063, 2009.

[39] Azin Sadat and Iris J Joye. Peak fitting applied to fourier transform infrared and raman spectroscopic analysis of proteins. *Applied Sciences*, 10(17):5918, 2020.

[40] DB Knowles, Andrew S LaCroix, Nickolas F Deines, Irina Shkel, and M Thomas Record Jr. Separation of preferential interaction and excluded volume effects on dna duplex and hairpin stability. *Proceedings of the National Academy of Sciences*, 108(31):12699–12704, 2011.